Marine electrical imaging reveals novel freshwater transport mechanism in Hawai‘i

Eric Attias[1*], Donald Thomas[1], Dallas Sherman[2], Khaira Ismail[3], and Steven Constable[4]

[1]Hawai‘i Institute of Geophysics and Planetology, School of Ocean and Earth Science and Technology, University of Hawai‘i at Mānoa, HI, USA
[2]Frontier Geosciences, BC, Canada
[3]University Malaysia Terrengganu, Malaysia
[4]Scripps Institution of Oceanography, University of California San Diego, CA, USA

*Corresponding author: Dr. Eric Attias; E-mail: attias@hawaii.edu.

Conventional hydrogeologic framework models employed to compute ocean island sustainable yields and aquifer storage neglect the complexity of the nearshore and offshore submarine environment. However, the onshore aquifer at the Island of Hawai‘i exhibits a significant volumetric discrepancy between high-elevation freshwater recharge and coastal discharge. In this study, we present a novel transport mechanism of freshwater moving from onshore to offshore through a multilayer formation of water-saturated layered basalts with interbedded low-permeability layers of ash/soil. Marine electromagnetic imaging reveals ~35 km of laterally continuous resistive layers that extend to at least 4 km from west of Hawai‘i's coastline, containing about 3.5 km^3 of freshened water. We propose that this newly discovered transport mechanism of fresh groundwater may be the governing mechanism in other volcanic islands. In such a scenario, volcanic islands worldwide can utilize these renew-

able offshore reservoirs as new water resources, which are considered more resilient to climate change-driven droughts.

INTRODUCTION

The global occurrence of vast offshore freshened groundwater reservoirs (*1–3*) may be utilized as a new resource to supply the increasing demand for water in the era of climate change-driven droughts (*4, 5*). Onshore aquifers are one of Hawai‘i's most critical natural resources, providing the vast majority of water for drinking, irrigation, domestic, commercial, and industrial needs (*6*). Volcanic eruptions, characterized by complex heterogeneous geology that includes lava flows, ash beds, faults, dikes, and lava tubes, form the young volcanic terrestrial aquifers situated on the Island of Hawai‘i (*6, 7*). Hydrogeologists typically assume that freshwater resources on volcanic islands are comprised of a shallow lens of freshwater floating on seawater (*8*). Hydrogeological studies often overlook formation heterogeneities, such as tight confining layers, despite their ability to extend freshwater resources far offshore (*9, 10*). In the nearshore land-to-sea transition zone, groundwater in Hawai‘i often presents a thin freshwater basal lens overlying seawater (*11–13*). Due to the nearly continuous subsidence of young Hawaiian volcanoes (*14, 15*) the Hualalai offshore region situated on the west flank of Hawai‘i island is composed of subaerial lava flow drapes partially covered by drowned coral reef terraces with low sediment content (*16*). The slope break that marks the western-most edge of the Hualalai subaerial shield lies at a depth of $\sim$800–950 m below current sea level and has an estimated age of $\sim$0.33 Ma (*16*).

Conventional hydrogeologic framework models for onshore aquifers assume thinning of the basal lens as the coastline is approached and freshwater heads decline, with dominant freshwater discharge to the ocean through coastal springs (*7*). However, for the Hualalai coastline, there is considerable evidence of submarine vents discharging freshwater to the ocean on a regional scale (*17–21*). Additionally, prior groundwater isotope studies (*22, 23*) suggest a significant volumetric discrepancy of ∼40% (18,000 m^3/d) in fresh groundwater recharge-to-discharge balance measured between the Hualalai volcano and its corresponding coastline. Investigation of the source of this discrepancy has motivated this study.

Marine controlled-source electromagnetic (CSEM) geophysical methods are sensitive to contrasts in bulk electrical resistivity (*24, 25*), primarily controlled by porosity and pore fluid properties of oceanic structures (*26, 27*). The substitution of conductive seawater with freshwater will increase the electrical resistivity of any geological formation (*28*). Various marine CSEM techniques were proven successful in imaging the electrical structure of continuous offshore freshened groundwater in different coastal sediment environments such as New Zealand (*29*), U.S. Atlantic coast (*2, 30*), and nearshore Israel (*31, 32*). In volcanic geology, where seawater-saturated basalts have resistivities of <10 Ωm (*33*), submarine freshwater-saturated basalts will manifest as 600–1100 Ωm resistive anomalies (*34*) embedded in a conductive background of seawater-saturated basalts.

Here, we present a novel multilayer transport mechanism of freshwater from onshore to offshore in Hawai‘i's complex geology. Using high-resolution marine CSEM imaging, we reveal the flow path, interconnectivity, and spatial distribution of deep submarine freshened groundwater layered bodies, and discover an extensive reservoir of purely freshwater within the submarine southern flank of the Hualalai aquifer, offshore west of Hawai‘i. Additionally, we provide a regional scale freshened/freshwater volumetric estimation. This is the first marine CSEM study that maps offshore submarine freshwater in a volcanic setting.

RESULTS

Multilayer electrical resistivity formation offshore the Island of Hawai‘i

To image the electrical formation of the submerged flank of the Hualalai volcano offshore west of Hawai‘i (Fig. 1), we used a newly developed surface-towed CSEM system (*35*). Pre-survey synthetic modelling demonstrates this CSEM system capability to image the electrical structure of the subsurface to a depth of ∼500 m below the seafloor, at water depths $<$100 m. This surface-towed system records spatially dense multi-frequency data, using four electromagnetic (EM) receivers distributed evenly over ∼1 km array (Fig. S1). Our marine survey included ten towlines parallel to the Hualalai terrestrial aquifer at incremental distances from the coastline (inline tows), and two perpendicular towlines (crossline tows), covering an offshore region of about 4 km wide and 40 km long, producing ∼200 km of continuous CSEM data (Fig. 1).

We performed isotropic and anisotropic inversions to the CSEM data using a standard deterministic nonlinear regularized 2-D inversion algorithm (*36*), producing 22 individual inversion models. These models show a sequence of alternating conductive and resistive layers that extend laterally ∼35 km parallel to the coastline with only moderate changes in depth (Fig. 2). The upper conductive layer extends from the seafloor to a depth of ∼100 m, presenting low electrical resistivity (∼0.2–1 Ωm), most likely resulting from the combination of seawater-saturated sediment, weathered ash, and basalts (Figs. 2 and 3). The lower conductive layer situated between ∼200–350 m depth, shows electrical resistivity of ∼0.8–2 Ωm (Fig. 3). Two resistive layers exist between ∼100–200 m and ∼350–500 m depth, presenting a resistivity range of ∼50–100 Ωm (Figs. 2 and 3). Based on the age of lavas associated with the Hualalai volcano (*16*), the age of these deep resistive layers are most likely at the range of a few hundred thousand years.

The alternating conductive/resistive horizontal layers revealed by our isotropic inversion models are most likely confined by low-permeability thin horizons of ash/soil (*37*), which formed above the Hualalai coastline and were armoured by lava flows before submergence (*16*). These low-permeability confining layers overlay freshened water layers, displacing more dense seawater to overlaying basaltic formations (Fig. 3). Such a pattern of alternating conductive and resistive horizontal layering is often caused by electrical anisotropy due to sediment grain alignment (*38*). However, our anisotropic inversion models present a similar layering pattern, thus confirming the capability of our isotropic inversions (Fig. 2) to resolve these anomalous resistive freshened groundwater bodies adequately.

The inversion models of both the inline and crosslines co-locate the resistive layers (Fig. 2). The inversion model of crossline 2 presents a deep anomalous resistive layer that extends up to a distance of at least 4 km offshore west of Hawai'i (Fig. 2).

Large-scale submarine freshwater reservoir

Parallel to Hualalai's southern flank, the inversion models of four consecutive survey lines consistently detected a deep large-scale anomalous resistive body that extends up to ∼2.5 km offshore south of Kailua-Kona (Fig. 2). This sizable resistor is at least ∼10 km long and ∼250 m thick, exhibiting a resistivity of ∼1000 Ωm (Fig. 2). The CSEM inversion model of survey line 2 South demonstrates the spatial extent and the highly anomalous resistivity of this large-scale submarine feature (Fig. 4). Such a high level of electrical resistivity indicates an extremely low salinity freshwater reservoir. Freshwater-saturated subaerial Mauna Kea basalts presented similar resistivities (*34*).

DISCUSSION

Resistivity to salinity calculation and freshened/freshwater volumetric estimation

Given the prevalence of fractured basaltic rocks in Hawai'i (*39*), we interpret the two resistive layers (∼50–100 Ωm) shown in Figs. 2 and 3 as freshened (moderately brackish) water-saturated basalts, with a salinity range of 3.2–6.8 ppt, calculated using Archie's law (*40*), assuming an average porosity of 20% and a cementation exponent of 2.57 [typical values for Hawai'i subaerial lava rocks (*41, 42*)], and the equations of state (*43*). Volumetric estimation on a regional scale suggests that these water-saturated basaltic layers accommodate at least 3.5 km^3 of freshened water, as calculated by Equation 1.

$$F_V = F_X \times F_Y \times F_Z \times \varphi \tag{1}$$

F_V represents the freshened water volume, F_X, the resistive layers average width (2 km, assuming continuous extension from the coastline), F_Y, the resistive layers horizontal length (35 km), F_Z, the resistive layers vertical extension (0.25 km), and φ denotes the average porosity (20%).

To estimate the salinity and volume of the large-scale freshwater reservoir detected offshore south of Kailua-Kona (Figs. 2 and 4), we applied Archie's equation (*40*) to calculate the formation pore fluid resistivity, using a formation bulk resistivity of $\sim$1000 Ωm (as derived from the CSEM inversions), cementation exponent of 2.57 and porosities of 20%±5%, as 5% change in porosity may significantly impact the estimate of pore water salinity (*29*). Note that such low porosities and high cementation values [representative to Hawai'i basalts (*42*)] suggest that a substantial volume of fresh pore fluid is required to yield a formation bulk resistivity of $\sim$1000 Ωm. Our calculation for formation pore fluid resistivity at porosities of 15, 20, and 25% yielded pore fluid resistivities of 7.5, 15, and 28 Ωm, respectively. Pore fluid resistivities of 7.5, 15, and 28 Ωm are equivalent to salinities of 0.62, 0.29, and 0.15 ppt, respectively, as calculated by the equations of state (*43*). Because water with a salinity $<$0.5 ppt is defined as pure freshwater (*44*), we consider this reservoir to be saturated entirely by freshwater at porosities of 20 and 25%. Thus, given the dimensions of this large-scale reservoir, we estimate it contains a freshwater volume of at least 1.25 and 1.56 km^3 at porosities of 20 and 25%, respectively. A porosity of 15% (salinity of 0.62 ppt) will result in reservoir volume of 0.93 km^3, saturated by freshened water. Summing the volumes of both the freshened water layers and the large-scale freshwater reservoir, we infer that the region mapped in this study offshore west of Hawai‘i contains a freshened/freshwater volume of at least 4.75 km^3, assuming a porosity of 20%.

We note that the offshore distance and depth extent of these freshened/freshwater reservoirs are not fully constrained due to the data acquisition limitations of the surface-towed CSEM system (*35*). Therefore, the inferred reservoirs may reach depths greater than 500 m and extend to the shelf edge ($\sim$6–8 km offshore). In this case, the reservoirs' volumes would be substantially higher than the minimum values estimated above. Such reservoirs of freshwater offshore Hawai‘i are most likely renewable, as implied from point-source fluxes of freshwater from the seafloor to the water column (*20, 21*).

Multilayer transport mechanism of deep submarine freshwater to offshore

Based on our CSEM inversion models, we present a new conceptual hydrogeologic model that describes the transport mechanism of freshwater from onshore to offshore at the Island of Hawai‘i (Fig. 5). In this region, rainwater that percolates through the porous basalts along the western flank of Hawai‘i Island recharges the Hualalai terrestrial aquifer. Less permeable ash/soil layers intercalated with the more permeable lava flows, intercept the freshwater as they infiltrate and migrate toward the coastline. If these low-permeability ash/soil layers are above the local water table, they act as perching formations. Whereas, below the water table, low-permeability layers serve as confining formations (*6, 7, 45, 46*). Hydrostatic head channels the freshwater below the confining formations, enabling its flow beneath sea level through permeable basalts while displacing gravitationally more dense seawater (Fig. 5). With high head levels, these freshwater flows may extend to the submerged flank of the volcanic edifice or alternately discharge into overlying saltwater saturated basalts if the confining formation terminates within the interior of the volcanic pile (*45, 46*).

Our model illustrates the flow of deep submarine freshwater to offshore Hawai‘i via a multilayer basaltic formation. Onshore borehole data acquired in the Hualalai terrestrial aquifer support this conceptual hydrogeological model (see below). However, the offshore component of the model is based solely on our electrical imaging, and thus, ideally, requires future validation by boreholes, seismic, and hydrogeological marine studies.

Observations of multilayer freshwater formations onshore the Island of Hawai‘i

Multiple onshore drilling studies conducted across the Island of Hawai‘i support the transport mechanism of freshwater from onshore to offshore, as illustrated by our conceptual model in Fig. 5. Salinity data obtained from the Kamakana borehole, located onshore Hualalai, in west Hawai‘i (Fig. 1), indicate the presence of a low-permeability layer at 300–315 m deep, which acts as a confining layer to a freshwater layer beneath (Fig. S5). The borehole depths of both the low-permeability and freshwater layers are consistent with the offshore depths of the low-permeability/freshwater layers shown in our inversion model of survey line 2 South (Fig. 4), located $\sim$3 km diagonally to Kamakana borehole (Fig. 2). Furthermore, several production/monitoring wells at higher elevations on the west flank of Hualalai have encountered either similar multi-layered aquifers (fresh-salt-fresh) or elevated freshwater hydrostatic heads more than sufficient to displace seawater to the depths observed by our offshore resistivity models.

In the east of Hawai‘i Island, resistivity surveys identified shallow resistive anomalies that represent high-elevation groundwater on the east flank of Mauna Kea (*34*). Additionally, resistivity log from the PTA2 borehole (situated west of Mauna Kea) exhibits a significant increase in resistivity at a depth of 1130 m, most likely associated with freshwater-saturated basaltic rocks (*47*). Drilling resistivity logs from borehole KP-1 located on the eastern flank of Hawai‘i detected a shallow freshwater basal lens underlain by saltwater-saturated rocks (*37,46*). Beneath these saltwater-saturated rocks, a deeper-buried freshwater aquifer exists between ∼320–520 m depth trapped below subsided soil horizon that marks the former surface of Mauna Kea, which the Mauna Loa basalt subsequently covered (*37, 48*). Below this ∼200 m thick aquifer, a zone with salinities similar to seawater exists at depths greater than 700 m. A borehole drilled 2 km away from KP-1 detected both the 320 m deep freshwater aquifer and additional deeper confined freshwater-saturated intervals to depths >3 km (*15*).

It is unlikely that the high resistivities observed in our CSEM models (Figs. 2–4) results from lithologic alterations in the submerged flanks of Hualalai. Because, drilling into the nearshore flanks of Mauna Kea, encountered typical subaerial lavas subsided by more than 1 km below current sea level (*15*). Given the similarity in ages of Hualalai with Mauna kea (*16*), we would expect typical shield building subaerial basalts within the resistive strata offshore.

Tracing the flow paths of dissolved silica in Hawai‘i demonstrated that the direct flow of submarine freshwater is a powerful mechanism for subsurface chemical weathering and solute flux from land to the ocean. Thus, calculations of weathering fluxes at young volcanic islands must include freshwater discharge to the ocean (*49*). Three-dimensional simulations of lava tubes (acting as conduits in a less permeable matrix of lava flows) suggest that submarine freshened groundwater accumulations occur offshore west of Hawai‘i, due to heterogeneous permeability and porosity (*50*). Therefore, lava tube conduits may be the primary source that supplies substantial volumes of water to the large-scale submarine freshwater reservoir detected by our inversion models (Figs. 2 and 4). Radiocarbon age dating of water samples collected from Hualalai coastal aquifer infers that deep freshwater reservoirs have prolonged cycle time, thus, more resilient to climate change (*51*).

Evidence for multilayer freshwater formations at other volcanic islands

To the best of our knowledge, no electromagnetic studies have been performed offshore at any other volcanic islands to confirm our proposed mechanism of freshwater transport from onshore to offshore via a multilayer basaltic formation. However, electromagnetic studies conducted in coastal areas of other volcanic islands such as Santa Cruz Island, Galapagos (*33*); Grande Comore Island, Comoros (*52*); Piton de la Fournaise volcano, Reunion (*53, 54*); Fogo Island, Cape Verde (*55*); and Maui Island, Hawai‘i (*41*) all present hydrogeological layered formations analogous to the submarine multilayer formation we revealed. For example, a three-dimensional airborne resistivity model of the Santa Cruz Island shows three main hydrogeological units that extend to a maximum depth of 300 m — a top unit of unsaturated-fractured basalt ($<$800 Ωm), followed by a unit of seawater-saturated basalt ($<$10 Ωm), and a deep freshwater-saturated basaltic unit with resistivity values ranging from 50–200 Ωm (*33*). The resistivity values of the seawater-saturated and freshwater-saturated units correspond to the top two layers presented in our inversion models, extending from the seafloor to a depth of $\sim$200 m (Figs. 2 and 3).

The studies above provide evidence for the existence of multilayer freshwater formations at the coastline of five other volcanic islands, thus supporting our findings' global-scale applicability. Consequently, we suggest that our unprecedented hydrogeologic conceptual flow model (Fig. 5) plays a more significant role than previously recognized in the transport mechanism of freshwater from onshore to offshore in volcanic islands. In such a scenario, renewable offshore freshwater reservoirs could potentially provide water to numerous volcanic islands worldwide.

CONCLUSIONS

This study reveals a novel mechanism that transports substantial volumes of freshwater from onshore aquifer to deep submarine aquifer offshore Hawai‘i via a multilayer basaltic formation. We propose that this transport mechanism may be the governing mechanism in other volcanic islands. Thus, such a mechanism may provide alternative renewable resources of freshwater to volcanic islands globally where the impacts of climate change decrease water availability. Our findings emphasize the importance of recognizing offshore submarine freshened/freshwater groundwater in future aquifer modelling to utilize water resources of volcanic islands. The large-scale submarine freshwater reservoir discovered here can potentially provide water to the Island of Hawaiʻi with high energetic efficiency and minimal impact on terrestrial and marine ecosystems.

METHODS

Data acquisition and processing

In September 2018, we collected ∼200 km of surface-towed CSEM data by towing a 40 m-long dipole antenna ∼0.5 m deep behind the survey boat at an average speed of 3.5 knots. The dipole antenna transmitted a 100 A current using a doubly symmetric square waveform (*56*) at a fundamental frequency of 1 Hz (sampling rate of 250 Hz), generating a source dipole moment of 5.09 kAm. Higher signal-to-noise (SNR) ratios characterize this waveform at higher frequencies than the standard square wave and other typical waveforms. The survey boat surface-towed four broadband electromagnetic (EM) receivers at offsets 268, 536, 804, 1072 m (Fig. S1). A Dorsal unit positioned 30 m behind the EM receivers array recorded the water depth and surface water conductivity and temperature. Each EM receiver recorded the inline horizontal electric field on a 2 m dipole positioned ∼0.65 m below the sea surface (Fig. S1). GPS units and electronic compasses logged the receivers' timing and positions, as well as orientations, respectively (*35*). The transmitter's and receivers' GPS units (positioned above sea level – directly exposed to satellites) provided continuous timing synchronization (accuracy of 10 ns), thus yielding stable phase values.

The recorded CSEM data were Fourier transformed to the frequency domain and stacked over 60 s intervals, which corresponds to ∼20 m lateral distance between transmitter stack points, producing amplitude and phase responses per each receiver as a function of position and frequency harmonics. The stacked amplitude and phase responses were then merged with the transmitter's and receivers' navigational information.

CSEM 2-D inversion scheme

For our CSEM inversion, we used the strongest harmonics of the doubly symmetric square waveform (*56*), which in this case, corresponds to high-frequency harmonics 3, 7, and 13 Hz. These frequencies produced quality data with high sensitivity to the interrogated depth beneath the seafloor. Thus, in combination with high data density, the frequencies yielded high-resolution inversion models. To invert the CSEM data for electrical resistivity, we employed the open-source MARE2DEM code, a 2-D nonlinear regularized inversion method that uses a parallel goal-oriented adaptive finite-element algorithm (*36*). MARE2DEM is based on the Occam's inversion, which searches for the smoothest model that fits the data to a predefined root-mean-square (RMS) target misfit (*57*).

The inversion-starting model discretization includes fixed parameters for a 10^{13} Ωm air layer, 0.2 Ωm half-space for the seawater column defined as free parameters, and 10 Ωm half-space for the sub-seafloor region. A high-resolution (2 m $\times$ 2 m) multi-beam system recorded the bathymetry used in the inversion modelling. Quadrilateral elements (*36*) discretized both the seawater column and the sub-seafloor (Fig. S3). The 40 m-long dipole transmitter and the 2 m-long towed CSEM receiver dipoles were modelled as finite dipole lengths. Our finite dipole inversions produced models with high sensitivity of the data to model parameters (Fig. S3). The inversions' horizontal-to-vertical roughness varies between 2 and 10 as a function of width-to-depth ratio. All the resistivity inversion models (Fig. 2) fit the data to an RMS misfit of $\sim$1.0. Table S1 details the parameterization and properties of the 2-D isotropic CSEM inversion models.

SUPPLEMENTARY MATERIALS

Supplementary material for this article is available at http://xxxxxxxxxxxxxxxx

REFERENCES AND NOTES

References

1. V. E. Post, J. Groen, H. Kooi, M. Person, S. Ge, W. M. Edmunds, Offshore fresh groundwater reserves as a global phenomenon. *Nature* **504**, 71 (2013).

2. C. Gustafson, K. Key, R. L. Evans, Aquifer systems extending far offshore on the US Atlantic margin. *Sci. Rep.* **9**, 1–10 (2019).

3. A. C. Knight, A. D. Werner, L. K. Morgan, The onshore influence of offshore fresh groundwater. *J. Hydrol.* **561**, 724–736 (2018).

4. T. H. Bakken, F. Ruden, L. E. Mangset, Submarine groundwater: a new concept for the supply of drinking water. *Water Resour. Manage.* **26**, 1015–1026 (2012).

5. J. J. Jiao, L. Shi, X. Kuang, C. M. Lee, W. W.-S. Yim, S. Yang, Reconstructed chloride concentration profiles below the seabed in Hong Kong (China) and their implications for offshore groundwater resources. *Hydrogeol. J.* **23**, 277–286 (2015).

6. S. B. Gingerich, D. S. Oki, Ground water in hawaii, *Tech. rep.*, US Geological Survey (2000).

7. D. S. Oki, Geohydrology and numerical simulation of the ground-water flow system of Kona, island of Hawaii, *Tech. rep.*, Geological Survey (US) (1999).

8. W. R. Souza, C. I. Voss, Analysis of an anisotropic coastal aquifer system using variable-density flow and solute transport simulation. *J. Hydrol.* **92**, 17–41 (1987).

9. M. Bakker, Analytic solutions for interface flow in combined confined and semi-confined, coastal aquifers. *Adv. Water. Resour.* **29**, 417–425 (2006).

10. J. F. Bratton, The importance of shallow confining units to submarine groundwater flow. *IAHS Publ.* **312**, 28 (2007).

11. H. T. Stearns, G. A. Macdonald, Geology and ground-water resources of the island of maui, hawaii. *Hawaii Div. Hydrogr.* p. 344 (1942).

12. S. B. Gingerich, C. I. Voss, Three-dimensional variable-density flow simulation of a coastal aquifer in southern Oahu, Hawaii, USA. *Hydrogeol. J.* **13**, 436–450 (2005).

13. S. B. Gingerich, Ground-water availability in the Wailuku Area, Maui, Hawai'i, *Tech. rep.*, US Geological Survey (2008).

14. J. G. Moore, D. Clague, Coastal lava flows from Mauna Loa and Hualalai volcanoes, Kona, Hawaii. *Bull. Volcanol.* **49**, 752–764 (1987).

15. E. M. Stolper, D. J. DePaolo, D. M. Thomas, Deep drilling into a mantle plume volcano: The Hawaii Scientific Drilling Project. *Scientific Drilling* **7**, 4–14 (2009).

16. B. Taylor, Shoreline slope breaks revise understanding of Hawaiian shield volcanoes evolution. *Geochem. Geophys. Geosyst.* **20**, 4025–4045 (2019).

17. T. K. Duarte, H. F. Hemond, D. Frankel, S. Frankel, Assessment of submarine groundwater discharge by handheld aerial infrared imagery: Case study of Kaloko fishpond and bay, Hawai‘i. *Limnol. Oceanogr.* **4**, 227–236 (2006).

18. A. G. Johnson, C. R. Glenn, W. C. Burnett, R. N. Peterson, P. G. Lucey, Aerial infrared imaging reveals large nutrient-rich groundwater inputs to the ocean. *Geophys. Res. Lett.* **35** (2008).

19. N. T. Dimova, P. W. Swarzenski, H. Dulaiova, C. R. Glenn, Utilizing multichannel electrical resistivity methods to examine the dynamics of the fresh water–seawater interface in two Hawaiian groundwater systems. *J. Geophys. Res.* **117**, 10.1029/2011JC007509 (2012).

20. H. Dulai, J. Kamenik, C. A. Waters, J. Kennedy, J. Babinec, J. Jolly, M. Williamson, Autonomous long-term gamma-spectrometric monitoring of submarine groundwater discharge trends in Hawaii. *J. Radioanal. Nucl. Chem* **307**, 1865–1870 (2016).

21. P. W. Swarzenski, H. Dulai, K. Kroeger, C. Smith, N. Dimova, C. Storlazzi, N. Prouty, S. Gingerich, C. R. Glenn, Observations of nearshore groundwater discharge: Kahekili Beach Park submarine springs, Maui, Hawaii. *J. Hydrol. Reg. Stud.* **11**, 147–165 (2017).

22. J. K. Fackrell, Geochemical evolution of hawaiian groundwater, Ph.D. thesis, University of Hawai‘i at Mānoa (2016).

23. C. Hudson, H. Dulai, A. El-Kadi, *Ocean Sciences Meeting, Portland, Oregon* (2018).

24. N. Edwards, Marine controlled source electromagnetics: principles, methodologies, future commercial applications. *Surv. Geophys.* **26**, 675–700 (2005).

25. S. Constable, Ten years of marine CSEM for hydrocarbon exploration. *Geophysics* **75**, 67–81 (2010).

26. P. Harris, L. MacGregor, Determination of reservoir properties from the integration of CSEM and seismic data. *First Break* **24**, 15–21 (2006).

27. L. MacGregor, J. Tomlinson, Marine controlled-source electromagnetic methods in the hydrocarbon industry: A tutorial on method and practice. *Interpretation* **2**, SH13–SH32 (2014).

28. F. Hoefel, R. Evans, Impact of low salinity porewater on seafloor electromagnetic data: A means of detecting submarine groundwater discharge? *Estuar. Coast. Shelf S.* **52**, 179–189 (2001).

29. A. Micallef, M. Person, A. Haroon, B. A. Weymer, M. Jegen, K. Schwalenberg, Z. Faghih, S. Duan, D. Cohen, J. J. Mountjoy, *et al.*, 3D characterisation and quantification of an offshore freshened groundwater system in the Canterbury Bight. *Nat. Commun.* **11**, 1–15 (2020).

30. D. Blatter, K. Key, A. Ray, C. Gustafson, R. Evans, Bayesian joint inversion of controlled source electromagnetic and magnetotelluric data to image freshwater aquifer offshore New Jersey. *Geophys. J. Int.* **218**, 1822–1837 (2019).

31. A. Haroon, K. Lippert, V. Mogilatov, B. Tezkan, First application of the marine differential electric dipole for groundwater investigations: A case study from Bat Yam, Israel. *Geophysics* **83**, B59–B76 (2018).

32. K. Lippert, B. Tezkan, On the exploration of a marine aquifer offshore Israel by long-offset transient electromagnetics. *Geophys. Prospect.* **68**, 999–1015 (2020).

33. N. d'Ozouville, E. Auken, K. Sorensen, S. Violette, G. de Marsily, B. Deffontaines, G. Merlen, Extensive perched aquifer and structural implications revealed by 3D resistivity mapping in a Galapagos volcano. *Earth Planet. Sc. Lett.* **269**, 518–522 (2008).

34. H. A. Pierce, D. M. Thomas, Magnetotelluric and audiomagnetotelluric groundwater survey along the Humuúla portion of Saddle Road near and around the Pohakuloa Training Area, Hawaii, *Tech. Rep. 2009–1135*, US Geological Survey (2009).

35. D. Sherman, P. Kannberg, S. Constable, Surface towed electromagnetic system for mapping of subsea Arctic permafrost. *Earth Planet. Sci. Lett.* **460**, 97–104 (2017).

36. K. Key, MARE2DEM: a 2-D inversion code for controlled-source electromagnetic and magnetotelluric data. *Geophys. J. Int.* **207**, 571–588 (2016).

37. D. Thomas, F. L. Paillet, M. Conrad, Hydrogeology of the Hawaii Scientific Drilling Project borehole KP-1: 2. Groundwater geochemistry and regional flow patterns. *J. Geophys. Res.* **101**, 11683–11694 (1996).

38. C. Ramananjaona, L. MacGregor, D. Andréis, Sensitivity and inversion of marine electromagnetic data in a vertically anisotropic stratified Earth. *Geophys. Prospect.* **59**, 341–360 (2011).

39. D. R. Sherrod, J. M. Sinton, S. E. Watkins, K. M. Brunt, Geologic map of the State of Hawaii. *US geological survey open-file report* **1089** (2007).

40. G. E. Archie, *et al.*, The electrical resistivity log as an aid in determining some reservoir characteristics. *Transactions of the AIME* **146**, 54–62 (1942).

41. B. R. Lienert, An electromagnetic study of maui's last active volcano. *Geophysics* **56**, 972–982 (1991).

42. A. Revil, A. Ghorbani, L.-S. Gailler, M. Gresse, N. Cluzel, N. Panwar, R. Sharma, Electrical conductivity and induced polarization investigations at Kilauea volcano, Hawai'i. *J. Volcanol. Geotherm. Res.* **368**, 31–50 (2018).

43. N. Fofonoff, Physical properties of seawater: A new salinity scale and equation of state for seawater. *J. Geophys. Res.* **90**, 3332–3342 (1985).

44. P. Bergstrom, Salinity methods comparison: Conductivity, hydrometer, refractometer. *The Volunteer Monitor* **14**, 20–21 (2002).

45. F. D. Tillman, D. S. Oki, A. G. Johnson, L. B. Barber, K. R. Beisner, Investigation of geochemical indicators to evaluate the connection between inland and coastal groundwater systems near Kaloko-Honokōhau National Historical Park, Hawaiʻi. *Applied geochemistry* **51**, 278–292 (2014).

46. D. M. Thomas, H. A. Pierce, N. C. Lautze, *AGU Fall Meeting Abstracts* (2017).

47. D. A. Jerram, J. M. Millett, J. Kück, D. Thomas, S. Planke, E. Haskins, N. Lautze, S. Pierdominici, Understanding volcanic facies in the subsurface: a combined core, wireline logging and image log data set from the PTA2 and KMA1 boreholes, Big Island, Hawaiʻi. *Sci. Dril.* **25**, 15–33 (2019).

48. D. M. Thomas, E. Haskins, E. Wallin, H. A. Pierce, New insights into the influence of structural controls affecting groundwater flow and storage within an ocean island volcano, mauna kea, hawaii. *AGU Fall Meeting Abstracts* **2015**, H31D–1446 (2015).

49. H. H. Schopka, L. A. Derry, Chemical weathering fluxes from volcanic islands and the importance of groundwater: The Hawaiian example. *Earth Planet. Sci. Lett.* **339**, 67–78 (2012).

50. P. Kreyns, X. Geng, H. A. Michael, The Influence of Connected Heterogeneity on Groundwater Flow and Salinity Distributions in Coastal Volcanic Aquifers. *J. Hydrol.* p. 124863.

51. B. Okuhata, A. El-Kadi, H. Dulai, D. Thomas, B. Popp, J. Lee, *Goldshmidt Virtual* (Goldshmidt, 2020).

52. A. Bourhane, J.-C. Comte, J.-L. Join, K. Ibrahim, *Active Volcanoes of the Southwest Indian Ocean* (Springer, 2016), pp. 385–401.

53. M. Descloitres, M. Ritz, B. Robineau, M. Courteaud, Electrical structure beneath the eastern collapsed flank of Piton de la Fournaise volcano, Reunion Island: Implications for the quest for groundwater. *Water Resour. Res.* **33**, 13–19 (1997).

54. J.-L. Join, J.-L. Folio, B. Robineau, Aquifers and groundwater within active shield volcanoes. Evolution of conceptual models in the Piton de la Fournaise volcano. *J. Volcanol. Geoth. Res.* **147**, 187–201 (2005).

55. M. Descloitres, R. Guérin, Y. Albouy, A. Tabbagh, M. Ritz, Improvement in TDEM sounding interpretation in presence of induced polarization. A case study in resistive rocks of the Fogo volcano, Cape Verde Islands. *J. Appl. Geophys.* **45**, 1–18 (2000).

56. D. Myer, S. Constable, K. Key, Broad-band waveforms and robust processing for marine CSEM surveys. *Geophys. J. Int.* **184**, 689–698 (2011).

57. S. C. Constable, R. L. Parker, C. G. Constable, Occam's inversion: A practical algorithm for generating smooth models from electromagnetic sounding data. *Geophysics* **52**, 289-300 (1987).

Acknowledgments: The authors would like to thank G. Jacobs, C. Voss, D. Eason, H. Dulai, N. Lautze, J. Perez, K. Amalokwu, V. Huvenne, J. Takahashi, C. Gustafson, K. Kerry, R.L. Evans, and Samer Naif for useful discussions. Additionally, we thank the scientific party of survey boat Huki Pono, the Natural Energy Laboratory of Hawaii Authority for survey support, and Tom Nance Water Resource Engineering for providing the borehole data. Finally, the authors thank editor Cin-Ty Lee, reviewer A. Haroon and two anonymous reviewers for their valuable suggestions that helped us improve the manuscript. **Funding:** This study was supported via the Hawai'i EPSCoR Program, funded by the National Science Foundation Research Infrastructure Improvement Award (RII) Track-1: 'Ike Wai: Securing Hawai'i's Water Future Award # OIA-1557349. **Author contributions:** E.A. designed the study, performed the 2-D CSEM inversion modelling and drafted the manuscript, which was revised by all co-authors. S.C. provided the surface-towed CSEM system and was a member of the external advisory board of this EPSCoR program. E.A. and D.S. executed the marine survey and processed the CSEM data. E.A., D.T., and S.C. interpreted the CSEM inversion models and constructed the conceptual model. K.I. processed the multi-beam bathymetry data. **Competing interests:** The authors declare no competing interests. **Data availability:** The CSEM data is available for download at https://doi.org/10.4211/hs.e0a7f2a216e9456a8567b850db1cf1f9. MARE2DEM is a parallel adaptive finite element code for two-dimensional forward and inverse modelling of electromagnetic data. MARE2DEM is available for download at https://mare2dem.bitbucket.io/.

Supplementary Materials

Figs. S1 to S5

Table S1

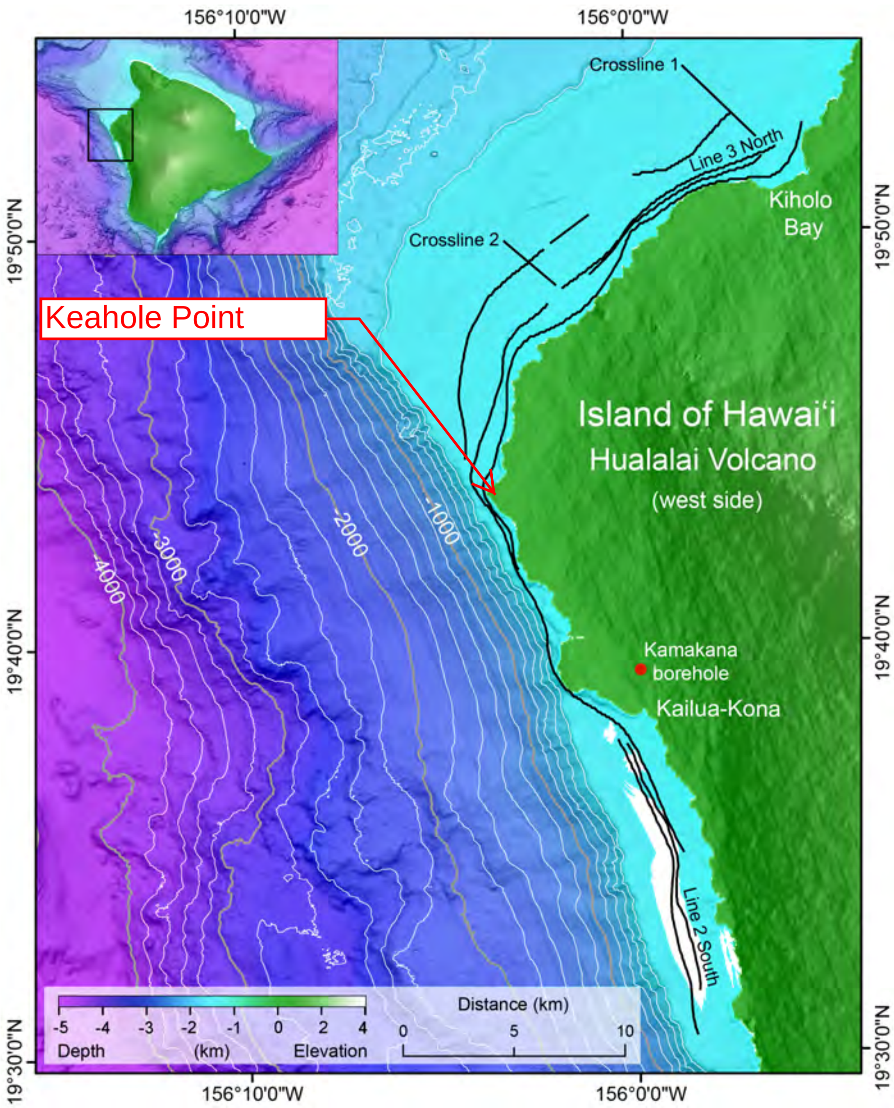

Fig. 1. Study area and survey layout. Map of the study area parallels to the Hualalai terrestrial aquifer at Kona, offshore west of Hawai‘i. The black lines denote the survey towlines (10 inlines, and two crosslines). White lines denote depth contours of 200 m, and grey lines the depth contours of 1000 m. Inset map: The Island of Hawai‘i, with black rectangle indicating the main map area. Areas with no bathymetry data are shown in white. Bathymetry data: Courtesy of Hawai‘i Mapping Research Group.

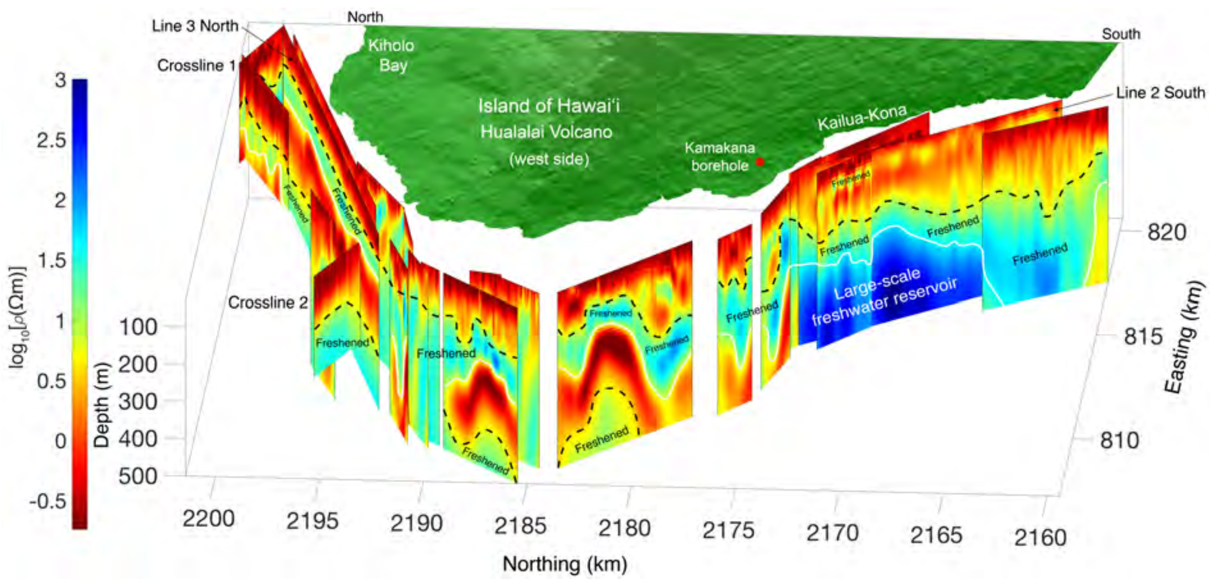

Fig. 2. Multilayer electrical resistivity formation offshore the Island of Hawai'i. Fence diagram showing 2-D isotropic CSEM inversion models of 20 discretized survey lines parallel to the Kona coastline and two crosslines. The color scale gives $\log_{10}[\rho(\Omega\text{m})]$, with blue and red colors corresponding to resistive and conductive features, respectively. Blue shaded areas starting at $\sim$100 meters depth denote horizontal layers of resistive anomalies that represent freshened water-saturated basalts, confined by low-permeability horizons of ash/soil (black-dashed lines). White lines denote the deeper boundary of these freshened horizontal layers. Spatially extensive and highly resistive area ($\sim$1000 Ωm) offshore Kailua-Kona represents a large-scale freshwater reservoir that extends from $\sim$250 to $\sim$500 depth. The models derived from the data acquired by three/four surface-towed CSEM receivers at 3, 7, 13 Hz (10 models), and 3, 7 Hz (12 models). The models' vertical exaggeration is approximately 16. Supplementary Table S1 presents the parameterization and properties of the inversion models.

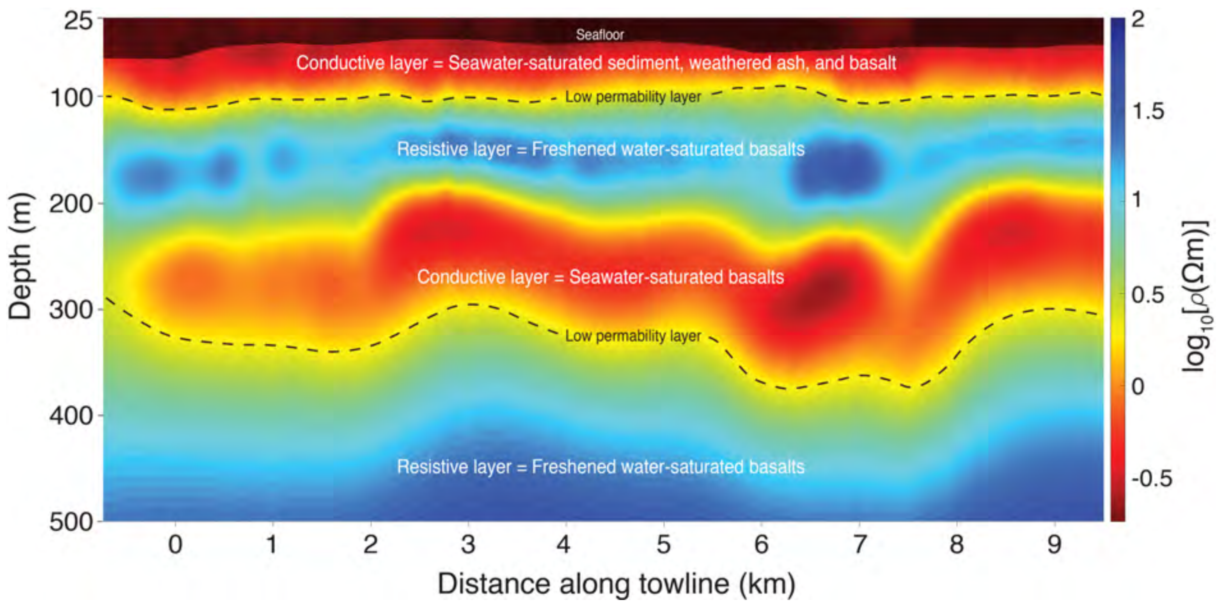

Fig. 3. Line 3 North inversion model. Model showing the electrical resistivity structure of line 3 North (see line location in Figs. 1 and 2). The colour scale show $\log_{10}[\rho(\Omega\text{m})]$. This multilayer inversion model is comprised of four lateral formations: Two conductive seawater-saturated basalts layers intermitted by two resistive freshened water-saturated basalts. low-permeability thin horizons of ash/soil (dashed lines) separate between the conductive and resistive layers. The model derived from the data acquired by three surface-towed CSEM receivers at 3 and 7 Hz. Inversion error floors: Amplitude = 7%, Phase = 4%. This inversion converged to an RMS misfit of 1.0 after 16 iterations. The model-to-data fits, and data sensitivities are shown in Supplementary Figs. S2 and S3, respectively.

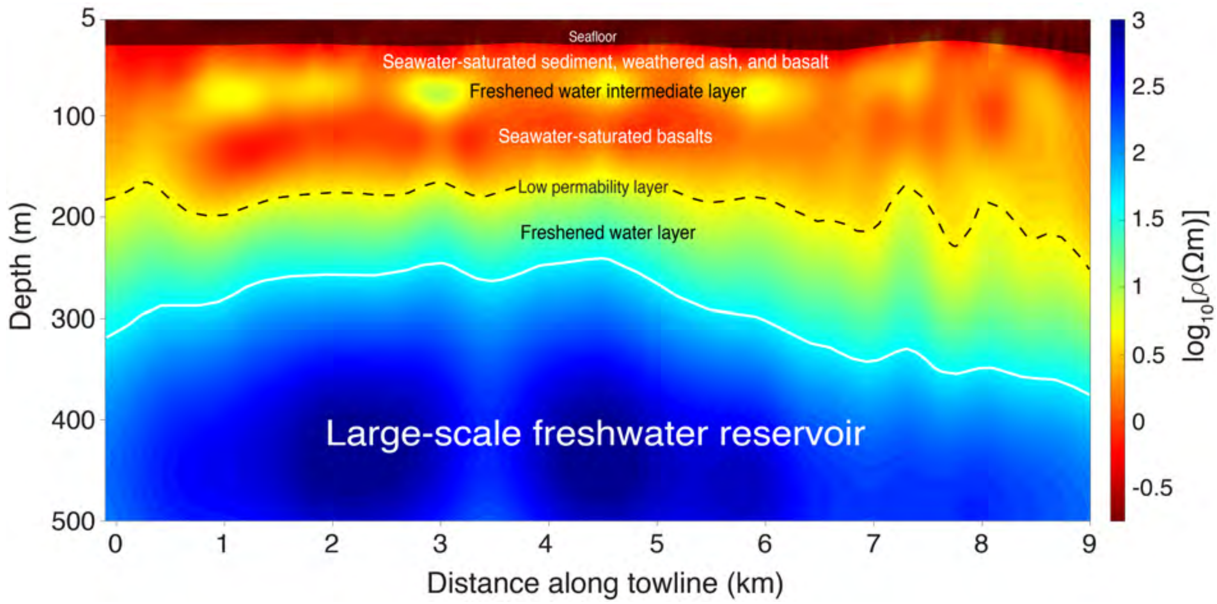

Fig. 4. Line 2 South inversion model. Model showing the electrical resistivity structure of line 2 South (see line location in Figs. 1 and 2). The colour scale show $\log_{10}[\rho(\Omega\text{m})]$. The deep and laterally continuous resistive body ($\sim$1000 Ωm) represents a large-scale freshwater reservoir (area bounded by a white line). low-permeability thin layer (black-dashed line) separates between the upper seawater-saturated (resistivity of $\sim$1–3 Ωm) basalts and the freshened water layer ($\sim$5–50 Ωm) situated between $\sim$190–320 m depths. A moderately resistive body ($\sim$5–10 Ωm) exists between $\sim$60–100 m depths, interpreted as an intermediate layer of freshened water. The conductive layer beneath the seafloor ($\sim$30–50 m depth) indicates seawater-saturated sediment, weathered ash, and basalts. The model derived from the data acquired by four surface-towed CSEM receivers at 3 and 7 Hz. Inversion error floors: Amplitude = 7%, Phase = 4%. This inversion converged to an RMS misfit of 0.99 after eight iterations. The model-to-data fits and normalized residuals are shown in Supplementary Fig. S4.

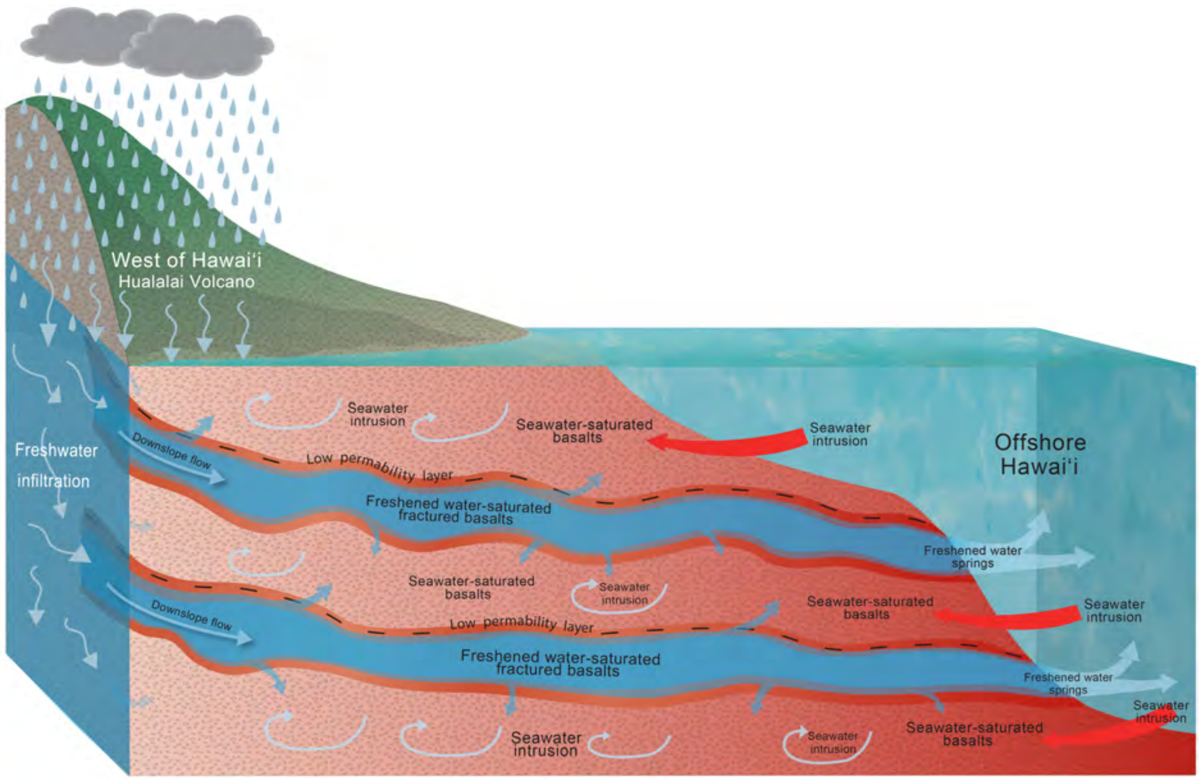

Fig. 5. Fresh groundwater onshore to offshore transport mechanism. Illustration showing a multilayer conceptual model of the transport mechanism of fresh groundwater from onshore to offshore in Hawai'i. Fresh groundwater recharge from rainfall infiltrates to the sub-surface basalts and migrate toward the coastline. low-permeability ash/soil layers intercept and perch the downslope migration (hydrostatic head driven) of freshwater in case that the freshwaters are above the water table. Below the water table, the low-permeability ash/soil layers act as confining formations. The freshwaters trapped below the confining formations flow thorough permeable fractured basalts and mix with seawater to form freshened groundwater while displacing gravitationally denser seawater. At the shelf edge, the freshened groundwater flows are released to the ocean as springs. Above and below the freshened water-saturated basaltic formations, seawater-saturated basalts exist as a result of seawater intrusions from the ocean towards the land.